

Uniaxial photomechanical motion in large diameter polydimethylsiloxane optical fibers with fluoropolymer claddings

Matthew Knitter,^a Louis Ferreira,^a D. Ryan Sheffield,^a Joseph Pusateri,^a
and Nathan J. Dawson^{a,b,c,*}

^aFlorida Polytechnic University, Department of Engineering Physics, Lakeland, Florida, United States

^bWashington State University, Department of Physics and Astronomy, Pullman, Washington, United States

^cYoungstown State University, Department of Physics, Youngstown, Ohio, United States

ABSTRACT. This study focuses on the photomechanical behavior of step-index optical fibers with a polydimethylsiloxane (PDMS) core and fluoropolymer claddings. The PDMS hosts dopant graphene nanoplatelets, which are heated when illuminated by visible light. Sample fibers were fabricated by drawing the doped resin into thin fluoropolymer tubing before the resin set. The individual motions of the core and cladding were observed to be coupled, which resulted in a relatively small photomechanical effect. Adding a castor oil lubricant between the core and cladding significantly increased the core's photomechanical strain. The large strain of the lubricated cores exhibited both irreversible and reversible photomechanical motion. Cycling the pump beam resulted in a fully reversible photomechanical piston that can be modeled by a linear response function to the incident pump beam.

© The Authors. Published by SPIE under a Creative Commons Attribution 4.0 International License. Distribution or reproduction of this work in whole or in part requires full attribution of the original publication, including its DOI. [DOI: [10.1117/1.JOM.4.1.013501](https://doi.org/10.1117/1.JOM.4.1.013501)]

Keywords: photomechanical effect; polymer optical fiber; graphene nanoplatelets; polydimethylsiloxane; actuator; piston; heat engine

Paper 23023G received Aug. 14, 2023; revised Jan. 13, 2024; accepted Jan. 20, 2024; published Feb. 8, 2024.

1 Introduction

Analogous to wires that guide the flow of charge carriers, optical fibers act as guides for light.¹ Just as the conductance, diameter, and work function of electrical wires affects charge carriers, the fiber core diameter and complex refractive index contrast between the core and cladding determines a multimode optical fiber's ability to guide light. Interest in optical fibers made from polymeric materials began in the 1980s.^{2–4} Polymer optical fibers can be easily doped with many organic molecules to add new functionality to optical fibers for use in photonic devices.^{5,6} Optically transparent, thermoplastic polymers are a common material of choice because they can be fabricated using the same melt-processing techniques as glass-based optical fibers.⁷ Like polymeric materials commonly used in optical fibers, polydimethylsiloxane (PDMS) is highly transparent in the visible spectrum and can be doped with organic molecules and inorganic particles. Researchers have recently investigated methods for fabricating optical fibers from PDMS.^{8–11}

The photomechanical effect is the observable deformation of an object when illuminated.^{12,13} The effect can be reversible^{14–16} or irreversible.^{17–19} Some well-studied mechanisms responsible for the photomechanical effect in solids include microscopic mechanisms such as

*Address all correspondence to Nathan J. Dawson, ndawson@floridapoly.edu

photoisomerization^{20–26} and photoreorientation^{27–30} as well as macroscopic mechanisms such as electrostriction^{31–33} and photothermal heating.^{34–39} Many materials can have multiple photomechanical response mechanisms.^{15,40} Fabricating photomechanical materials into specific geometries has resulted in many devices, such as soft-robotic actuators,^{41–44} electric generators,^{45–49} power meters,⁵⁰ optical switches,^{51,52} self-oscillators,⁵³ and biomimetic actuators.^{54–57} Photomechanical devices have also been shown to move over water,^{58,59} across terrain,^{32,60–63} and through the air.⁶⁴ Photomechanical devices can also be used as components in larger photomechanical systems with both series^{65–67} and parallel^{68,69} configurations.

Doped PDMS has been the focus of many photomechanical studies^{70–76} due to its large coefficient of thermal expansion.⁷⁷ Because of the recent research interest in both PDMS optical fibers and the photomechanical effect in PDMS composites, we investigated the photomechanical motion of doped PDMS in an optical fiber geometry. Photomechanical optical fibers can be directly pumped from micro-optical sources and serve as optical-mechanical transducers. Some of the optical fibers presented in this study behave like light-driven pistons, which could be used as actuators for linear motion or a component of a light-fueled engine.

In this study, prefabricated fluoropolymer tubes act as a mold and cladding for large-diameter optical fibers. Poly(tetrafluoroethylene-co-hexafluoropropylene) (FEP) and polytetrafluoroethylene (PTFE) were chosen as the cladding materials. The low refractive index of FEP makes it an ideal candidate for large-diameter optical fibers.⁷⁸ The PTFE tubing has a higher refractive index,⁷⁹ and the opaqueness causes scattering at the core/cladding interface; however, the relatively low surface energy⁸⁰ (useful for “non-stick” applications) was identified as a target for study based on potential device applications. Many photomechanical materials have been illustrated by doping PDMS with various forms of carbon particles such as carbon nanotubes,^{81,82} carbon nanoparticles,^{83,84} reduced graphene oxide,^{85,86} and graphene nanoplates.⁸⁷ Graphene nanoplates (GNP) were used in this study due to their high thermal conversion efficiency.⁸⁸

2 Experiment

Photomechanical samples were fabricated by mixing GNP (≤ 4 nm thickness) into Sylgard 184 base at a concentration of 0.0083 wt.%. Multiple rounds of shear mixing and bath sonication were performed until a homogeneous mix was achieved. The cross-linker was then introduced with the manufacturer’s recommended 1:10 volume ratio and mixed for 5 min. The final mixture was placed in a desiccator under vacuum for 20 min until no visible air bubbles remained.

The pre-cured, viscous liquid was drawn into either FEP or PTFE tubing. Histograms of the FEP and PTFE tubing inner diameters captured from 50 cross-sectional images each are respectively shown in Figs. 1(a) and 1(b), where both histograms follow a normal distribution. The mean inner diameter of the FEP tubing was approximately 1.60 mm with a standard deviation of 20 μm . The PTFE tubing inner diameter had a mean of 1.58 mm with a standard deviation of 20 μm . During the drawing process, one end of a tube was submerged into the pre-cured elastomer mixture while the other was held at vacuum pressure. The tubing filled with uncured

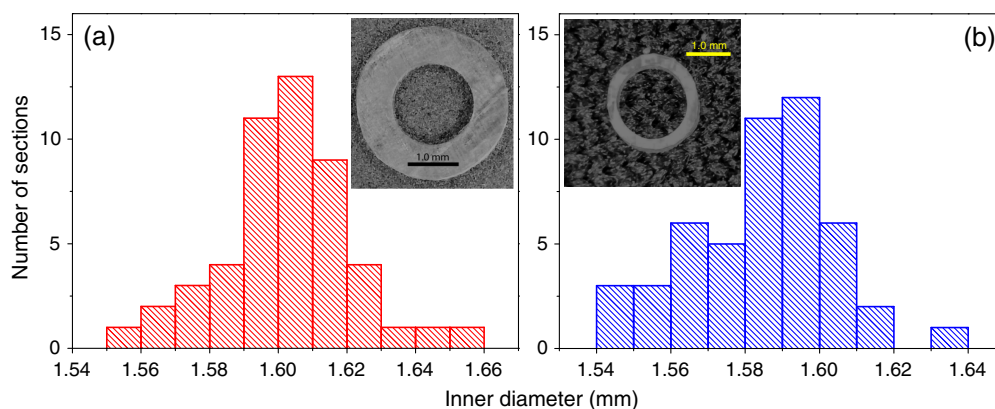


Fig. 1 Histogram of inner diameters for the (a) FEP and (b) PTFE tubing taken from images of cross-sectional slices.

GNP-PDMS was then placed in an oven and cured at 100°C for ~30 min. The cured fibers were placed on a bench in ambient conditions for > 2 h prior to further experimentation. The resultant samples were broadband-absorbing optical fibers with doped PDMS cores which were clad with either an FEP or PTFE fluoropolymer. The typical fiber fabricated with this method had a total length of ~15 cm before being sectioned into smaller units for experimentation. Longer fibers could be drawn using this method; however, the rate at which the PDMS is drawn through the tubing is reduced when per length increment drawn into the tubing.

To remove adhesion and reduce friction between the fiber core and cladding, a third type of optical fiber was fabricated. This new type of fiber was fabricated with a lubricant layer between the core and cladding regions, and it was fabricated using the following technique. First, PTFE-clad fibers with GNP-PDMS cores were fabricated using the process stated above. A small ~1 cm length of PTFE tubing was left vacant at one end. Then, a small slit ~0.5 cm in length was cut through the vacant end of the PTFE tubing using a razor blade. Afterward, the cladding was split into two sections at one end of the fiber. The two cladding pieces at the split end of the fiber were pulled away from each other which tore away the cladding from the entire core resulting in two semi-circular strips of PTFE cladding, which were discarded, and a standalone GNP-PDMS fiber core. Next, FEP tubing was pre-filled with castor using vacuum pressure, and the standalone GNP-PDMS core was submerged in castor oil. After being submerged in castor oil, one end of the core was inserted into the FEP tubing. For the final step, the far end of the FEP tubing was held at vacuum pressure which drew the remaining length of the core into the FEP tubing. Images from various stages of the process are shown in Fig. 2(a).

We fully expected to measure a strain in the free-standing GNP-PDMS fibers upon removing the PTFE core during the processing steps of the lubricated samples. Multiple fibers were measured, and no length change was observed, which indicates a negligible amount of internal stress in the GNP-PDMS core after curing in the PTFE tubing.

For photomechanical experiments, a class IIIb, 445 nm, diode laser was passed through neutral density (ND) filters and a relay-controlled laser shutter. The clad optical fiber was positioned in a hole which was bored through a black-painted aluminum block and then mounted using a thumb screw via a tapped hole facing perpendicular to the length of the fiber. The

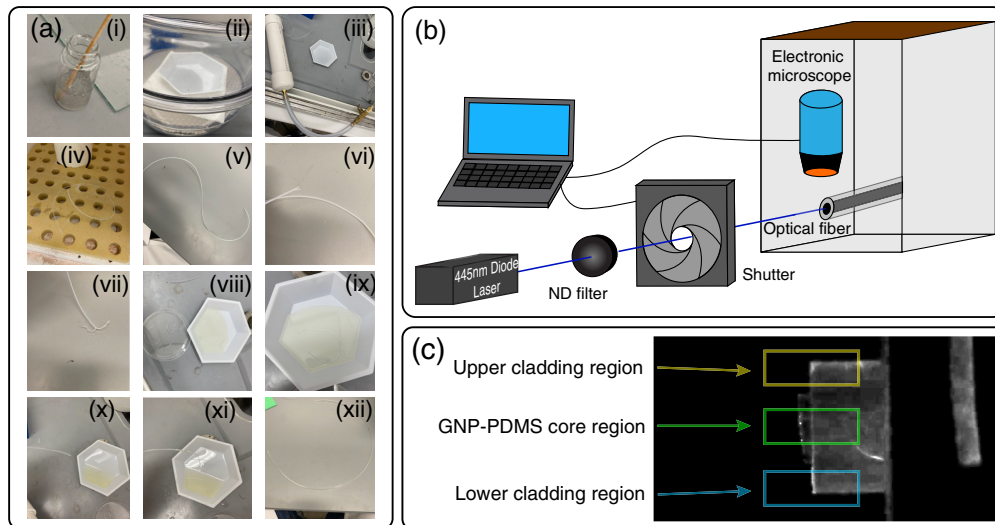


Fig. 2 (a) After the GNPs are homogenized in the base (i) crosslinker is added and mixed, (ii) the mixture is desiccated, (iii) PTFE tubing is filled under vacuum pressure, (iv) and the fiber is cured resulting in (v) the GNP-PDMS/PTFE fiber. Then, (vi) a fiber end is scored with a razor blade, (vii) the cladding is pulled away from the core, and (viii) the free-standing GNP-PDMS fiber is ready to be submerged in castor oil. (ix) The free-standing fiber is submerged in oil, (x) FEP tubing is attached to the vacuum, and (xi) the freestanding fiber is drawn into the FEP tubing, which (xii) results in a GNP-PDMS/Oil/FEP fiber. (b) The main experimental setup for characterizing photomechanical optical fibers. (c) The regions for left-edge detection shown over the top of a lubricated GNP-PDMS/FEP optical fiber image during an experiment.

cladding was subject to clamped condition by the hole/screw apparatus approximately half of a centimeter from the unilluminated end of the fiber. A microscope was directed vertically downward as illustrated in Fig. 2(b). The red channel was used to take micrographs, and two 550 nm long-pass filters were placed between the fiber and the microscope to reduce channel mixing of the blue laser light. A weak white light source illuminated the sample and holder. The sample and microscope were encased in an acrylic box to reduce dust particles that could scatter light near the fiber end. A 3/8" hole was drilled into the box to allow the laser beam to pass through. The incident beam illuminated a ~ 1 mm diameter spot centered on the fiber core. An Ophir PD300-UV sensor measured the pump power before each experiment after the beam was passed 1 O.D. ND filter.

A preliminary micrograph was recorded, and the shutter was opened for 135 s. The shutter was closed for 180 s to complete the first experimental cycle. Each experiment was cycled three times and the microscope camera collected images periodically at 2 Hz over a 945 s interval. There were 1890 images recorded and analyzed per experiment. A script imported all images after each experiment and measured the change in pixels of the core and cladding edges relative to the fiber mount. Figure 2(c) shows a contrast-enhanced image taken during experimentation and highlights the regions for detecting changes in the left-most edge points.

3 Results

The attenuation of light through the fiber was measured by coupling low-intensity laser light into the fiber and measuring the transmitted light for fibers of various lengths. All fibers exhibited an exponential decay as a function of length. The results follow the Beer-Lambert law

$$\frac{\partial I}{\partial z} = -\alpha I, \quad (1)$$

for homogeneous materials. Here, I is the intensity, z is the length through the material, and α is the attenuation coefficient. The multimode, undoped, PDMS/FEP fiber shown in Fig. 3 has an attenuation coefficient of (0.46 ± 0.10) dB/cm. The difference in the undoped PDMS cores is due to scattering introduced by the PTFE cladding. The attenuation coefficient for the undoped PDMS/PTFE fiber was measured to be (1.6 ± 0.3) dB/cm. Assuming similar losses from leakage in multimode fibers of similar step indices, the additional loss in the undoped PDMS/PTFE fiber is scattering from the white opaque PTFE tubing. The scattering loss caused by the PTFE cladding for light traveling through undoped PDMS is ~ 1.1 dB/cm. Note that the values are given in decibels, but the fits were performed using an exponential decay with the natural Euler number e as the base and later converted to decibels from Nepers.

The GNP-PDMS optical fibers had attenuation coefficients that were significantly larger than the undoped PDMS fibers as shown by the fit lines in Fig. 3. The attenuation coefficients for optical fibers with GNP-PDMS cores were (5.7 ± 0.2) dB/cm, (6.8 ± 0.6) dB/cm, and (6.6 ± 0.2) dB/cm for the respective FEP-clad, PTFE-clad, and lubricated FEP-clad samples.

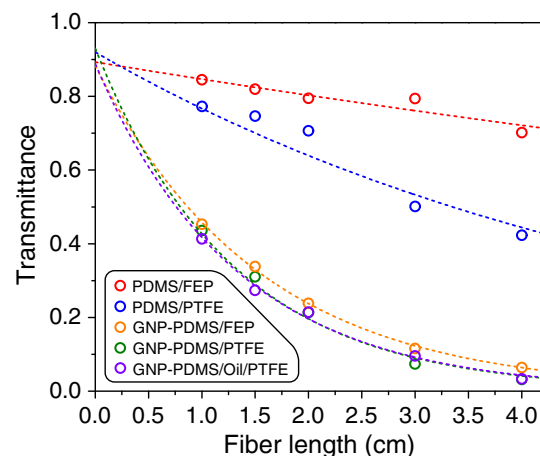


Fig. 3 Power transmittance of optical fibers as a function of length.

From the results of the attenuation measurements for the undoped PDMS clad with transparent FEP and the undoped PDMS clad with white opaque PTFE, it is clear that scattering at the PDMS-PTFE interface in GNP-PDMS/PTFE fibers causes the increase in attenuation. The additional loss in the GNP-PDMS/Oil/FEP fibers, caused by the introduction of the higher-index castor oil layer, was smaller than observed in the GNP-PDMS/PTFE fibers, but the attenuation was still ~ 0.9 dB/cm greater than that observed in the GNP-PDMS/FEP fibers. Tracing all attenuation curves back to the air/fiber interface (fiber length $\rightarrow 0$), all fiber types (undoped PDMS and GNP-PDMS cores) are observed to have similar interfacial coupling losses, $\sim 10\%$.

The first photomechanical experiment measured the photomechanical response of a GNP-PDMS/FEP fiber. After images were taken, the location of the measured core+cladding motion [center/green boxed region shown in Fig. 2(b)] and the location of the measured cladding motion in the surrounding regions were recorded as functions of time. After each three-cycle experiment, the pump beam power was changed to check the response as a function of pump power. The sample was 1.5 cm in length, meaning more than 30% of the pump beam's power was transmitted through the sample without being absorbed.

The rate by which the optical fiber heats and cools depends on the thermal properties of the materials used for the core and cladding as well as their dimensions. If the entire core+cladding system was uniformly heated, then Newton's law of cooling for a single system would apply; however, there are two distinct, cylindrically symmetric regions in the optical fiber. Let us assume that most of the heat generated in the core flows through the core/cladding interface. The inner boundary of the cladding then increases in temperature while heat diffuses through the cladding's volume. The cladding's outer surface increases in temperature, which cools via convective boundary conditions at the cladding/air interface.

We can make a few more simplifying approximations for the FEP-clad fibers. Let us consider:

1. the ambient temperature T_{amb} does not change during the experiment,
2. effects from heat flow along the fiber are negligible in comparison to heat flow through the core/cladding boundary,
3. the overwhelming majority of heat generated in the core conducts to the cladding, and
4. the cladding diffuses heat through it much faster than the rate by which it cools.

Under these circumstances we can write a set of coupled, first-order, differential equations in time for the core temperature T_{core} and cladding temperature T_{clad} , which are of the form

$$\frac{dT_{\text{core}}}{dt} = -a_1(T_{\text{core}} - T_{\text{clad}}) + bP(t), \quad (2)$$

$$\frac{dT_{\text{clad}}}{dt} = -a_2(T_{\text{clad}} - T_{\text{amb}}) + a_1(T_{\text{core}} - T_{\text{clad}}), \quad (3)$$

with the initial conditions,

$$T_{\text{core}}(t = 0) = T_{\text{clad}}(t = 0) = T_{\text{amb}}, \quad (4)$$

where a_1 and a_2 denote the coefficients of heat transfer between the respective core/cladding and cladding/air interfaces, P is the laser power, and b is the photothermal coefficient.

The time-dependent solution for the core temperature from Eqs. (2) and (3) is biexponential when $P(t)$ is a positive constant after the power is stepped on at $t = 0$. If the amplitude of one of the terms is much greater than the other, then we can simply approximate a heat kernel as a single exponential in time after averaging over the system's volume. Likewise, the cladding can also be reduced to a single exponential with similar arguments. These approximations of either the core or cladding result in the fiber's average temperature asymptotically approaching a maximum via an exponential growth function shortly after the shutter is opened. Similarly, when the pump beam is blocked, all temperatures decay exponentially to the ambient temperature. The growth and decay exponential behaviors have the same rate constant per material. The strain response to a change in temperature is assumed to be much quicker than the thermal response to a step function from photothermal heating by a CW laser source. Thus, a linear response function can be used to model the change in length of the core and cladding as a function of time.

Large viscoelastic effects are commonly observed in pristine elastomeric materials. The greatest transients typically leave the system after the first cycle, and therefore, the linear response function is assumed to best model the photomechanical motion starting from the second cycle in new samples. The length change of the core and cladding are both modeled by the linear response function

$$\Delta L(t) = \int_{-\infty}^t R(t-t')P(t')dt', \quad (5)$$

where $R(t)$ is the response function and $\Delta L = L - L_0$ with L being the length at some time t and L_0 being the length when the fiber's temperature is equal to the ambient temperature. The linear response function for the length change is of the form

$$R(t) = Ae^{-at}, \quad (6)$$

where A and a are constants.

Figure 4(a) shows the motion of the fiber core's edge as a function of time for two different pump powers. The response function curve from Eqs. (5) and (6) fit the length change data starting the moment the shutter was opened on the second cycle. There were two fit parameters, a and $\frac{AP_0}{a}$, where P_0 is the pump beam's power during a given experiment. All fits seem to match the time-dependent data reasonably well, which justifies the earlier approximation that resulted in the form of the response function given by Eq. (6).

Figures 4(b) and 4(c) plot the fitted parameters as functions of the pump power. The decay parameter a appears to be reasonably independent of the pump power, as expected. The core's decay constant is an order of magnitude greater than the cladding's decay constant. The trend for $\frac{AP_0}{a}$ is linear for the cladding material. The amplitude for the core appears to be nonlinear in an unexpected way, but the uncertainties are much greater due to the relatively small motion of the edge and the noise from edge detection.

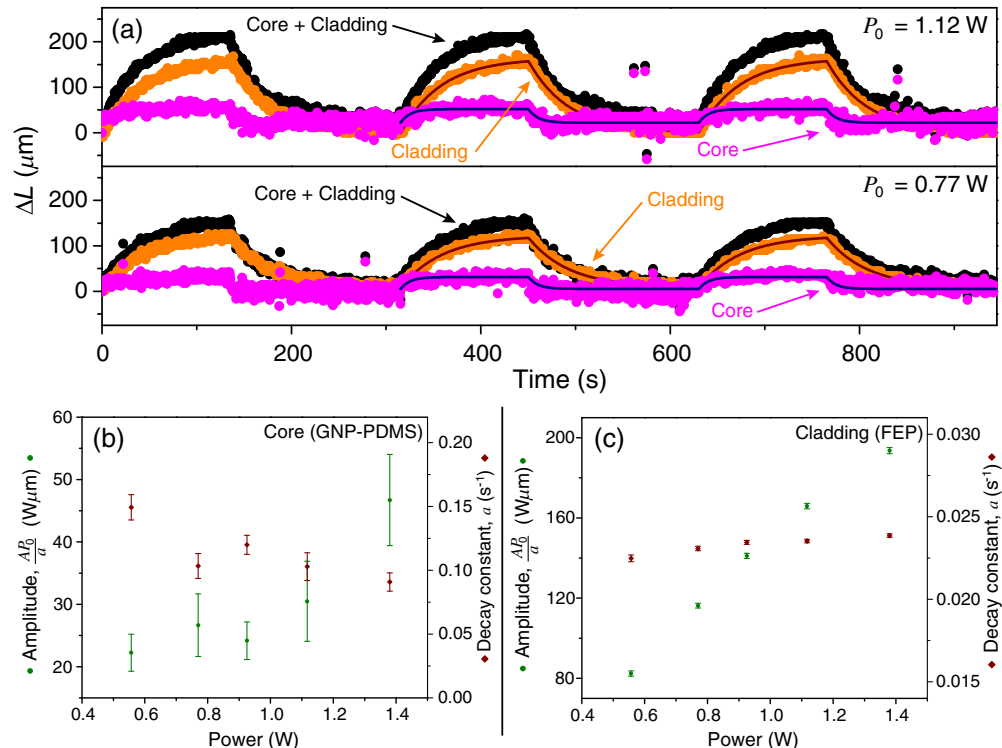


Fig. 4 (a) Core and cladding expansion at the incident beam interface for an unlubricated GNP-PDMS/FEP optical fiber as a function of time at two different pump powers. The (b) GNP-PDMS core and (c) FEP cladding edges were fit with a response function with parameters shown in the respective plots.

A single exponential response fit the observed data quite well for the 1.5 cm GNP-PDMS/FEP fiber, which is indicative of a simplified Newton cooling model, $\frac{dT}{dt} = -a(\Delta T) + bP_0$, where $\Delta T = T - T_{\text{amb}}$. It is clear that the steady-state solution occurs when $\frac{dT}{dt} = 0$ which means that the asymptotic temperature is $\Delta T_{\text{max}} = bP_0/a$. Here, $b = \gamma/(m_{\text{core}}C_{\text{core}} + m_{\text{clad}}C_{\text{clad}})$, where m is the mass and C is the specific heat for the core and cladding. The fraction of beam power absorbed is γ which is 0.66 for the 1.5 cm GNP-PDMS/FEP fiber from the data provided in Fig. 3. Based on the dimensions of the fiber and densities^{89,90} of the materials, the mass are calculated to be $m_{\text{core}} \sim 30$ mg and $m_{\text{clad}} \sim 160$ mg. Also, the specific heats are known to be $C_{\text{core}} \sim 1.5 \text{ kJ kg}^{-1}\text{C}^{-1}$ ⁸⁹ and $C_{\text{clad}} \sim 1 \text{ kJ kg}^{-1}\text{C}^{-1}$,⁹⁰ which gives an estimate, $b \sim 3.2^\circ\text{C}/\text{J}$. We assume that the length change response to an increase in temperature is much faster than the temperature change response to the incident pump beam. Therefore, the temperature change response to the pump beam is essentially the same as the length change response to the pump beam. Therefore, let us use $a = 0.024 \text{ s}^{-1}$ at $P_0 = 1.38 \text{ W}$ for the cladding material length change as a function of time to approximate the time constant for the temperature change, which results in $\Delta T_{\text{max}} = bP_0/a \sim 180^\circ\text{C}$. Note that this high ΔT_{max} value was never realized in experiments due to the slow response time for the cladding material; rather, it is an extrapolated value at $t \rightarrow \infty$. From the cladding strain curves shown in Fig. 4(a), the strain reached $\sim 90\%$ of the asymptotic value. For a linear approximation to thermal expansion, the maximum increase in experimental temperature was $\sim 162^\circ\text{C}$, which occurred when the sample was illuminated with the maximum power beam of 1.38 W for the maximum amount of time, 135 s. Starting from room temperature, the greatest increase in temperature was below the maximum operating temperature of 200°C listed for both FEP and PDMS.^{77,90}

The coefficient of linear thermal expansion β is defined by the equation $\Delta L = \beta L_0(\Delta T)$. Because the exponential growth is slow as shown by the example curves in Fig. 4(a), the data must be extrapolated to $t \rightarrow \infty$ from the fitting parameters given in Figs. 4(b) and 4(c). Using these values and taking the limit where $\Delta L_{\text{max}} = \beta L_0 \Delta T_{\text{max}}$ gives an estimated value of $\beta \sim 10^{-4}\text{C}^{-1}$. This estimated value of the linear coefficient of thermal expansion is closer to the value attributed to FEP.⁹⁰ It is much smaller than Sylgard 184's linear coefficient of thermal expansion in free-standing films, $\sim 3.4 \times 10^{-4}\text{C}^{-1}$.⁵⁰ Therefore, adhesion between the core and cladding plays a major role in the amount of photomechanical motion observed in the GNP-PDMS/FEP optical fibers. Indeed, we spent a great deal of effort trying to free the fiber from the FEP cladding by forcing core-sized metallic rods into an end of the fiber; all attempts were unsuccessful. Note that we can immediately see the pinning/adhesion effect by observing the disparity in the parameter a between the core and cladding. Basically, the GNP-PDMS quickly expands until stressed caused by adhesion between the core and cladding keep the GNP-PDMS material from further expanding relative to the core—the entire core + cladding cross-section at the fiber's end expands at a slower rate dominated by the much more massive and voluminous FEP cladding material.

The GNP-PDMS core was also studied using a PTFE cladding. The inner diameter of PTFE tubes was nearly identical to those made from FEP; however, the outer diameter was much smaller as shown in the inset of Fig. 1(b). The thinner walls of the PTFE tube can transfer heat out of the system much faster than the FEP cladding. Additionally, scattering at the PDMS-PTFE interface along the fiber can cause increased absorption near the cladding, which in turn can cause increased heat generation near the edges of the fiber's core.

The length change results for GNP-PDMS/PTFE fibers are shown in Fig. 5. One of the most striking features observed in the PTFE-clad optical fibers was the core's apparent contraction relative to the cladding. As with the previously studied fibers, the left-most edges in the middle of the images were used to detect the combined core and cladding movement whereas the upper and lower regions were used to only detect the cladding motion. After subtracting the cladding movement from the combined core + cladding motion, a contraction of the GNP-PDMS core relative to the cladding was consistently reported across all samples and over all cycles.

The thermal and mechanical properties of the FEP and PTFE claddings affected the photo-mechanical behavior of the core due to the adhesion which occurred while curing. Curing the samples in PTFE and removing the tubing allowed for free standing GNP-PDMS fibers. Castor oil was chosen as the lubricant because of the large molecular sizes of triglycerides which do not swell PDMS.⁹¹

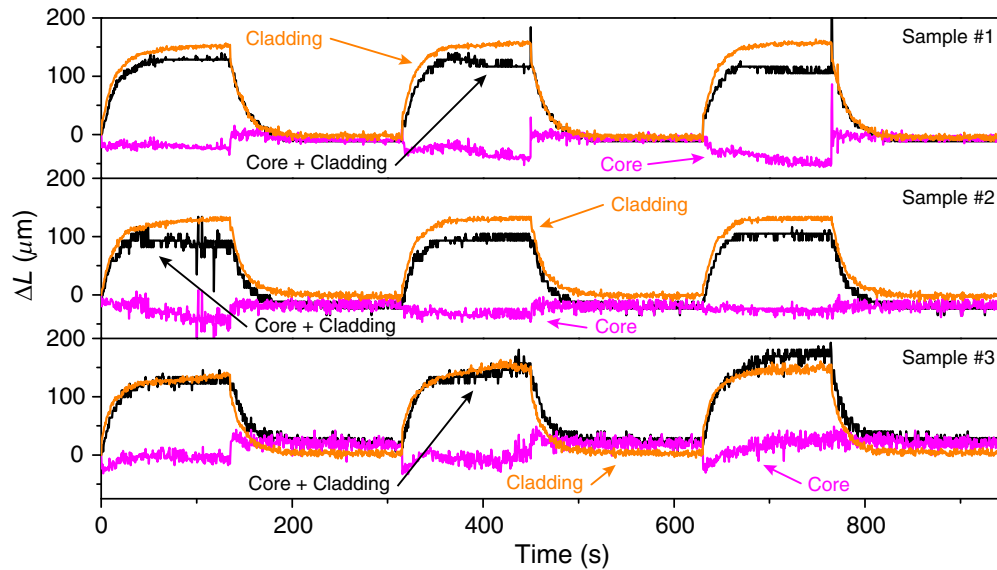


Fig. 5 The motion as a function of time for incident-beam edges of three different GNP-PDMS/PTFE optical fibers.

The photomechanical behavior for two GNP-PDMS/Oil/FEP optical fibers of different lengths is shown in Fig. 6. The initial response of a pristine sample is the most glaring artifact in both plots. A very large and irreversible motion occurs after initially opening the laser shutter. An initial motion of over 1 mm was observed for the 4 cm optical fiber. The photomechanical motion shows significant stability and reversibility after the first cycle. This initially large motion was observed in all samples.

Regarding length dependence for the irreversible process, the core of the 1 cm-long fiber exhibited a large, but still smaller motion during the first cycle. The amount of irreversible strain was directly proportional to the power absorbed by the sample. The 1 cm fiber absorbed about 3/5 of the pump beam power while the 4 cm fiber absorbed nearly all of the pump beam. Figure 6 shows that the irreversible strain observed in the 1 cm GNP-PDMS/Oil/FEP fiber after the first cycle was about 7/10 of the irreversible strain exhibited by the 4 cm fiber. The 4 cm is longer, where the response time for the first cycle is slower for that sample. Extrapolating the curves in

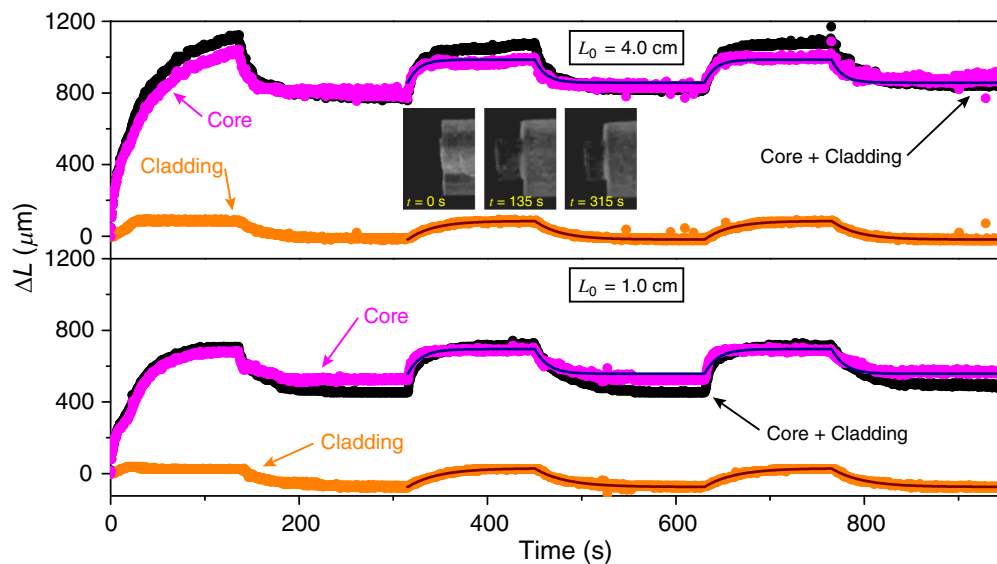


Fig. 6 The edge position of two GNP-PDMS/Oil/FEP optical fibers as functions of time. The inset on the upper plot shows images of the optical fiber before illumination, immediately after the shutter was turned off for the first time, and after the completion of the first cycle.

Fig. 6 shows a trend in which the final irreversible strain of the 1 cm fiber would be closer to 3/5 of the strain in the 4 cm fiber.

The most interesting aspect of the motion in the GNP-PDMS/Oil/FEP fibers shows up in the following cycles. First, there was no worm-like crawling out of the cladding. Instead, the motion became reversible. Another interesting aspect of the reversible motion was the amplitude. Both the 1.5 and 4 cm samples were subject to the same incident power ($P_0 = 1.38$ W) with the same beam shape and positioning. The amplitude of the reversible motions are approximately same despite the length change. From response model fits, we see that $\frac{\Delta P_0}{a} = (131 \pm 9) \mu\text{m W}$ for the 4 cm-long sample and $\frac{\Delta P_0}{a} = (141 \pm 7) \mu\text{m W}$ for the 1 cm-long sample, where the amplitudes overlap within uncertainty. One might expect that the reversible motions such that the 1 cm-long fiber would have an amplitude that was about 3/5 of the 4 cm-long sample; however, the amplitudes observed in these nearly-reversible motions were roughly the same.

4 Discussion

Multimode, doped, optical fibers were fabricated with PDMS as the core material. Because fluoropolymers have a relatively low refractive index, PTFE and FEP were chosen as the cladding material. A small photomechanical motion was observed in GNP-PDMS/FEP optical fibers, where the central region of the PDMS core's surface on the incident edge expanded. This motion was well-characterized by a simple exponential response function. The core motion had a response time that was an order of magnitude faster than the FEP cladding's response to end-pumping the core. No motion was observed within the precision of the microscope on the opposite end of the fiber for FEP- and PTFE-clad samples when no lubricant was used between the core and cladding.

Interestingly, GNP-PDMS/PTFE optical fibers showed a negative photomechanical motion of the core relative to the PTFE cladding's motion. We did not address the magnitude or the response time. Once the core receded a few pixels, only the cladding was visible to the camera and therefore the extent of the recession into the PTFE material was unattainable. The PTFE tubing was soft, thin-walled, and exhibited greater expansion relative to the FEP tubing, where scattering-induced local heating near the PDMS-PTFE interface and the thickness of the tubing are assumed to be responsible for the observed differences between the photomechanical behavior in GNP-PDMS/PTFE and GNP-PDMS/FEP fibers.

Photomechanical motion of large-diameter optical fibers fabricated from doped PDMS could be problematic for many applications. There are some actuation applications, however, that could benefit from the photomechanical behavior observed in these materials. A large initial photomechanical effect was observed after adding some lubricating oil between the GNP-PDMS core and FEP cladding. Photomechanical motion was observed to be reversible after the initial transient behavior was removed by cycling the pump on/off. The GNP-PDMS/Oil/FEP fiber's end that was opposite of the incident beam did irreversibly recede into the cladding when observing with the naked eye; however, no quantitative transient data was available for analysis due to the direction in which the fiber-end moved and the geometry of the microscope setup.

The large reversible photomechanical motions in the GNP-PDMS/Oil/FEP fibers were surprisingly similar in amplitude between the 1 cm-long and 4 cm-long fiber. There are many possible mechanisms responsible for the nearly identical amplitude as recovered via curve fitting. In fact, the system is quite complicated due to the uncertainty in materials, post-processing, and effects from irreversible transients. Heterogeneities in both the PTFE and FEP tubing can cause narrow and wide locations in the core. There are likely heterogeneities in thermal and mechanical properties in the cured PDMS material at various scales. Coupling these uncertainties with long-time scales and transient behavior can result in large-scale uncertainties in the fiber's photomechanical behavior.

Samples of GNP-PDMS/Oil/PTFE optical fibers were also prepared. In every case, oil oozed out of the ends of the sample upon illumination. The edge of the core and cladding materials were not distinguishable from the oil edges in these samples, and therefore, no image analysis was performed on their photomechanical behavior.

In an attempt to create PTFE-clad optical fibers with large photomechanical responses, GNP-PDMS/Oil/PTFE fibers were fabricated in the same manner as the GNP-PDMS/Oil/

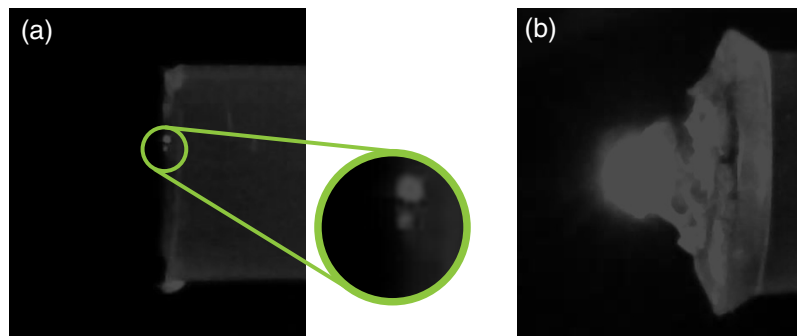


Fig. 7 (a) Reactions caused by diode laser hot spots. (b) Rare occasion of grinder complete optical fiber failure at high intensity.

FEP fibers. Every attempt at using these fibers resulted in oil leaking emerging from the fiber end when illuminated by the pump beam. We were unable to distinguish between the fiber core's edge and the oil surrounding through the microscope images. The white opaque cladding of the PTFE cladding scatters light at the inner boundary unlike the FEP fibers. The effects of this scattering on the propagation of light through the fiber can be seen in Fig. 3 for the PDMS/PTFE fiber when compared to the PDMS/FEP fiber. Scattering from the PTFE inner wall increases the local light intensity, which in turn increases the heat generation near the thin oil layer. Thus, this increased heat generation caused the consistent oil leakage from the GNP-PDMS/Oil/PTFE fiber ends in these samples. Note that oil also emerged from the end of GNP-PDMS/Oil/FEP samples in some cases, but those were infrequently encountered.

This study used a diode laser to pump doped optical fibers at relatively high CW intensity. In doing so, we sometimes observed chemical reactions at the incident edge of the fiber. Figure 7(a) shows two small “jets” of burning material forming at the edge of the GNP-PDMS core. These would sometimes appear at the highest power used in this study, $P_0 = 1.38$ W, where hot spots from the focused laser speckle pattern would form. Care was taken to avoid these in edge detection analysis.

There were two instances in which optical fibers catastrophically failed; in these two samples, a lensing effect caused the fibers to become superheated near the incident edge. The incident boundary in both fibers greatly expanded while expelling ignited material in what appeared to be a miniature explosion. The moment just after the material ignited and expulsion began is shown in Fig. 7(b). The FEP material was irreversibly deformed in both cases with the edge bending outward.

5 Conclusion

This research aimed to investigate the photomechanical motion of doped PDMS in an optical fiber geometry, focusing on the interaction between core and cladding materials. The experimental results demonstrated that GNP-PDMS cores in FEP-clad optical fibers exhibited a detectable photomechanical response characterized by a simple exponential response. The core's response time in FEP-clad fibers was significantly greater than the cladding. The study also explored the application of lubricating oil between the core and cladding, which resulted in large irreversible photomechanical strains followed by reversible motion when cycling the pump on/off. Sample-to-sample variations were identified in fibers with complex fabrication steps, which necessitates future processing methods with greater precision.

The investigation into GNP-PDMS cores with thin PTFE cladding revealed an intriguing phenomenon—a negative photomechanical motion of the core relative to the cladding. The study also highlighted potential challenges associated with high-intensity laser pumping, such as irreversible reactions and catastrophic failures at the incident edge of the optical fibers. Overall, this research sheds light on the complex interplay between material properties, geometry, and experimental conditions in determining the photomechanical behavior of optical fibers. Further exploration is warranted to better understand and control the photomechanical motion in step-index optical fibers.

Disclosures

The authors declare no conflicts of interest.

Code and Data Availability

Data produced by this work are available at <https://doi.org/10.17632/pmc8fwxcv3.1> (accessed on 12 August 2023).

Acknowledgments

This material is based upon work supported by the National Science Foundation (Grant No. 2226956).

References

1. D. Marcuse, *Principles of Optical Fiber Measurements*, Elsevier Science, Saint Louis (2014).
2. T. Kaino, "Absorption losses of low loss plastic optical fibers," *Jpn. J. Appl. Phys.* **24**(12), 1661–1665 (1985).
3. T. Yamashita et al., "Light scattering measurement in PMMA optical fibers," *Jpn. J. Appl. Phys.* **26**(11), L1797–L1799 (1987).
4. Y. Koike et al., "Gradient-index polymer materials and their optical devices," *Polym. Eng. Sci.* **29**(17), 1200–1204 (1989).
5. A. Tanaka et al., "New plastic optical fiber using polycarbonate core and fluorescence-doped fiber for high temperature use," *Fiber Integr. Opt.* **7**(2), 139–158 (1988).
6. M. G. Kuzyk, U. C. Paek, and C. W. Dirk, "Guest-host polymer fibers for nonlinear optics," *Appl. Phys. Lett.* **59**(8), 902–904 (1991).
7. M. G. Kuzyk, *Polymer Fiber Optics: Materials, Physics, and Applications*, Optical Science and Engineering, Vol. **117**, CRC/Taylor & Francis, Boca Raton (2007).
8. I. Martinec, D. Pudis, and M. Chalupova, "Technology for the preparation of pdms optical fibers and some fiber structures," *IEEE Photonics Technol. Lett.* **26**(14), 1446–1449 (2014).
9. J. Guo, M. Niu, and C. Yang, "Highly flexible and stretchable optical strain sensing for human motion detection," *Optica* **4**(10), 1285–1288 (2017).
10. R. Kiessling et al., "Gravity-drawn silicone filaments: production, characterization, and wormlike chain dynamics," *CS Appl. Mater. Interfaces* **9**(46), 39916–39920 (2017).
11. M. Llera et al., "Few-mode elastomeric optical fibers," *Opt. Mater. Express* **11**(7), 2288–2299 (2021).
12. T. J. White, *Photomechanical Materials, Composites, and Systems: Wireless Transduction of Light into Work*, John Wiley & Sons (2017).
13. M. G. Kuzyk and N. J. Dawson, "Photomechanical materials and applications: a tutorial," *Adv. Opt. Photonics* **12**(4), 847–1011 (2020).
14. X. Ye and M. G. Kuzyk, "Photomechanical response of disperse red 1 azobenzene dye-doped PMMA polymer fiber," *Opt. Commun.* **312**, 210–215 (2014).
15. B. Zhou et al., "Theoretical and experimental studies of photomechanical materials," *J. Opt. Soc. Am. B* **36**(6), 1492–1517 (2019).
16. Y. Li et al., "Morphing of stiffness-heterogeneous liquid crystal elastomers via mechanical training and locally controlled photopolymerization," *Matter* **5**(12), 4332–4346 (2022).
17. J. Sodhi and I. Rao, "Modeling the mechanics of light activated shape memory polymers," *Int. J. Eng. Sci.* **48**(11), 1576–1589 (2010).
18. J. Zhang et al., "Shape memory and self-healing materials from supramolecular block polymers," *Polymer* **134**, 35–43 (2018).
19. A. Ravi and K. M. Sureshan, "Tunable mechanical response from a crystal undergoing topochemical dimerization: instant explosion at a faster rate and chemical storage of a harvestable explosion at a slower rate," *Angew. Chem., Int. Ed.* **57**(30), 9362–9366 (2018).
20. T. Guo et al., "Regimes in the response of photomechanical materials," *Appl. Sci.* **12**(15), 7723 (2022).
21. W. Li et al., "Dynamic optical grating based on a photomechanical molecular crystal," *Adv. Opt. Mater.* **11**(6), 2202190 (2023).
22. Y. Yue et al., "Molecular twisting affects the solid-state photochemical reactions of unsaturated ketones and the photomechanical effects of molecular crystals," *Chem. Eur. J.* **29**(7), e202203178 (2023).
23. M. Singh et al., "Excellent photo actuation in crystal-polymer composite by transfer of mechanical energy," *Chem. Eng. J.* **464**, 142665 (2023).
24. V. Toshchevikov and M. Saphiannikova, "Photo-ordering and deformation in azobenzene-containing polymer networks under irradiation with elliptically polarized light," *Processes* **11**(1), 129 (2023).

25. J. Lall and H. Zappe, “Understanding photomechanical behavior of liquid crystalline-based actuators,” *Macromol. Mater. Eng.* **308**(5), 2300063 (2023).
26. M. Lakshmipathi et al., “Mechanically elastic and light-induced bending of acylhydrazone-based photo-switch crystal,” *Cryst. Growth Des.* **23**(7), 4939–4945 (2023).
27. S. Bian, D. Robinson, and M. G. Kuzyk, “Optically activated cantilever using photomechanical effects in dye-doped polymer fibers,” *J. Opt. Soc. Am. B* **23**(4), 697–708 (2006).
28. Y. Chen et al., “Enhanced ordering and efficient photoalignment of nanostructures in block copolymers enabled by halogen bond,” *Macromolecules* **53**(4), 1486–1493 (2020).
29. Z. Ghorbanishiadeh et al., “Photothermal and reorientational contributions to the photomechanical response of DR1 Azo dye-doped PMMA fibers,” *Appl. Sci.* **12**(1), 315 (2021).
30. Z. Sekkat, “Photomechanical solid polymers: model for pressure and strain induced by photoisomerization and photo-orientation,” *Appl. Sci.* **13**(1), 321 (2023).
31. K. Uchino and M. Aizawa, “Photostrictive actuator Using PLZT ceramics,” *Jap. J. Appl. Phys.* **24**, 139–141 (1985).
32. K. Uchino, “Ceramic actuators: principles and applications,” *MRS Bull.* **18**, 42–48 (1993).
33. K. Uchino, “Photostrictive actuators based on piezoelectrics,” in *Advanced Piezoelectric Materials – Science and Technology*, 2nd ed., K. Uchino, Ed., pp. 755–785, Elsevier (2017).
34. N. J. Dawson et al., “Experimental studies of the mechanisms of photomechanical effects in a nematic liquid crystal elastomer,” *J. Opt. Soc. Am. B* **28**, 1916–1921 (2011).
35. N. J. Dawson et al., “Modeling the mechanisms of the photomechanical response of a nematic liquid crystal elastomer,” *J. Opt. Soc. Am. B* **28**(9), 2134–2141 (2011).
36. W. Wei et al., “A NIR light-triggered pyroelectric-dominated generator based on a liquid crystal elastomer composite actuator for photoelectric conversion and self-powered sensing,” *RSC Adv.* **8**(71), 40856–40865 (2018).
37. Z. Ghorbanishiadeh et al., “Effect of disperse red 1 azobenzene dye doping and annealing on the thermo-mechanical and photomechanical properties of PMMA fibers,” *Appl. Sci.* **12**(16), 7991 (2022).
38. J. Wang et al., “Light-powered self-sustained oscillators of graphene oxide/liquid crystalline network composites showing amplitude and frequency superposition,” *ACS Appl. Mater. Interfaces* **14**(13), 15632–15640 (2022).
39. B. F. Lui et al., “Performance of a photothermal actuator based on molecular absorbers dissolved in eicosane,” *Sens. Actuator A: Phys.* **360**, 114514 (2023).
40. H. Wu et al., “Photothermally promoted photoisomerization of naphthopyran-based dyes to achieve sensitive photodeformation under sunlight,” *ACS Mater. Lett.* **5**(3), 753–761 (2023).
41. C. Zhu et al., Chapter 9 in *Photomechanical Liquid Crystal Polymers and Bioinspired Soft Actuators*, pp. 233–256, John Wiley & Sons, Ltd (2020).
42. Y. Chen et al., “Light-driven bimorph soft actuators: design, fabrication, and properties,” *Mater. Horiz.* **8**(3), 728–757 (2021).
43. Z. Yu et al., “Fast-response bioinspired near-infrared light-driven soft robot based on two-stage deformation,” *ACS Appl. Mater. Interfaces* **14**(14), 16649–16657 (2022).
44. Z. Hu et al., “Bioinspired helical-artificial fibrous muscle structured tubular soft actuators,” *Sci. Adv.* **9**(25), eadh3350 (2023).
45. J. J. Wie et al., “Photopiezoelectric composites of azobenzene-functionalized polyimides and polyvinylidene fluoride,” *Macromol. Rapid Commun.* **35**(24), 2050–2056 (2014).
46. R. Tang et al., “Optical pendulum generator based on photomechanical liquid-crystalline actuators,” *ACS Appl. Mater. Interfaces* **7**(16), 8393–8397 (2015).
47. Y. Xiong et al., “A solar actuator based on hydrogen-bonded azopolymers for electricity generation,” *J. Mater. Chem. A* **6**(8), 3361–3366 (2018).
48. D. Zhao and Y. Liu, “Photomechanical vibration energy harvesting based on liquid crystal elastomer cantilever,” *Smart Mater. Struct.* **28**(7), 075017 (2019).
49. H.-Y. Chen et al., “Secondary energy conversion devices based on cylindrical liquid crystalline elastomer-assisted triboelectric generators,” *ACS Appl. Electron. Mater.* **4**(4), 1415–1426 (2022).
50. F. Sun et al., “All-optical method of determining laser power from the photomechanical effect,” *Appl. Sci.* **12**(21), 10708 (2022).
51. D. J. Welker and M. G. Kuzyk, “Optical and mechanical multistability in a dye-doped polymer fiber Fabry-Perot waveguide,” *Appl. Phys. Lett.* **66**(21), 2792–2794 (1995).
52. D. J. Welker and M. G. Kuzyk, “All-optical switching in a dye-doped polymer fiber Fabry-Perot waveguide,” *Appl. Phys. Lett.* **69**(13), 1835–1836 (1996).
53. L. Zhou et al., “Light-powered self-oscillation in liquid crystal elastomer auxetic metamaterials with large volume change,” *Int. J. Mech. Sci.* **254**, 108423 (2023).
54. O. M. Wani, H. Zeng, and A. Priimagi, “A light-driven artificial flytrap,” *Nat. Commun.* **8**, 15546 (2017).

55. J. Hu et al., “A programmable and biomimetic photo-actuator: a composite of a photo-liquefiable azobenzene derivative and commercial plastic film,” *J. Mater. Chem. C* **6**(40), 10815–10821 (2018).
56. X. Li et al., “Photo-activated bimorph composites of Kapton and liquid-crystalline polymer towards biomimetic circadian rhythms of *Albizia Julibrissin* leaves,” *J. Mater. Chem. C* **7**(3), 622–629 (2019).
57. J. Sun et al., “Gecko-and-inchworm-inspired untethered soft robot for climbing on walls and ceilings,” *Cell Rep.* **4**(2), 101241 (2023).
58. M. Camacho-Lopez et al., “Fast liquid-crystal elastomer swims into the dark,” *Nat. Mater.* **3**, 307–310 (2004).
59. S. Ma et al., “A light-activated polymer composite enables on-demand photocontrolled motion: transportation at the liquid/air interface,” *Angew. Chem. (Int. Ed.)* **58**(9), 2655–2659 (2019).
60. L. Yu and H. Yu, “Light-powered tumbler movement of graphene oxide/polymer nanocomposites,” *ACS Appl. Mater. Interfaces* **7**(6), 3834–3839 (2015).
61. J. Mu et al., “Origami-inspired active graphene-based paper for programmable instant self-folding walking devices,” *Sci. Adv.* **1**(10), e1500533 (2015).
62. Y. Norikane and K. Saito, “Crawling motion of crystals on solid surfaces by photo-induced reversible crystal-to-melt phase transition,” in *Mechanically Responsive Materials for Soft Robotics*, H. Koshima, Ed., pp. 83–103, Wiley-VCH Verlag GmbH & Co. KGaA, Weinheim (2020).
63. T. Zhao et al., “Phototactic miniature soft robots with terrain adaptability,” *Adv. Mater. Technol.* **7**(9), 2101660 (2022).
64. T. Song et al., “Supramolecular hydrogen bond enables Kapton nanofibers to reinforce liquid-crystalline polymers for light-fueled flight,” *Nano Energy* **87**, 106207 (2021).
65. N. J. Dawson et al., “Cascading of liquid crystal elastomer photomechanical optical devices,” *Opt. Commun.* **284**, 991–993 (2011).
66. N. J. Dawson et al., “Integration of liquid crystal elastomer photomechanical optical devices,” *Proc. SPIE* **8475**, 84750B (2012).
67. A. S. Kuenstler, H. Kim, and R. C. Hayward, “Liquid crystal elastomer waveguide actuators,” *Adv. Mater.* **31**(24), 1901216 (2019).
68. D. Zhao and Y. Liu, “Programmable liquid crystal elastomer matrix through photomechanical responses,” *J. Appl. Polym. Sci.* **137**(34), 48997 (2020).
69. D. Niu et al., “Reconfigurable shape-morphing flexible surfaces realized by individually addressable photo-actuator arrays,” *Smart Mater. Struct.* **30**(12), 125032 (2021).
70. J. Loomis and B. Panchapakesan, “Dimensional dependence of photomechanical response in carbon nanostructure composites: a case for carbon-based mixed-dimensional systems,” *Nanotechnology* **23**(21), 215501 (2012).
71. D. Niu et al., “Reversible bending behaviors of photomechanical soft actuators based on graphene nanocomposites,” *Sci. Rep.* **6**, 27366 (2016).
72. Leeladhar et al., “Graphene-polydimethylsiloxane/chromium bilayer-based flexible, reversible, and large bendable photomechanical actuators,” *Smart Mater. Struct.* **26**(9), 095030 (2017).
73. W. Jiang et al., “Controllable actuation of photomechanical bilayer nanocomposites for in vitro cell manipulation,” *Carbon* **139**, 1048–1056 (2018).
74. Leeladhar and J. P. Singh, “Human skin-inspired multiresponsive actuators based on graphene oxide/polydimethylsiloxane bilayer film: bi-directional transformation of semi-tube into plane sheet/tube under different stimuli,” *Smart Mater. Struct.* **29**(7), 75022 (2020).
75. J. D. López-Lugo et al., “Photomechanical polymer nanocomposites for drug delivery devices,” *Molecules* **26**(17), 5376 (2021).
76. P. Satapathy et al., “Porous nanocarbon particles drive large magnitude and fast photomechanical actuators,” *J. Nanostruct. Chem.* **12**(2), 235–248 (2022).
77. The Dow Chemical Company, Technical Data Sheet: SYLGARD 184 Silicone Elastomer, 2017, <https://pdf1.alldatasheet.com/datasheet-pdf/view/1425043/ETC/SYLGARD-184.html>
78. K.-I. Tsunoda et al., “The use of poly(tetrafluoroethylene-co-hexafluoropropylene) tubing as a waveguide capillary cell for liquid absorption spectrometry,” *Appl. Spectrosc.* **44**(1), 163–165 (1990).
79. W. E. Hanford and R. M. Joyce, “Polytetrafluoroethylene,” *J. Am. Chem. Soc.* **68**(10), 2082–2085 (1946).
80. S. Rhee, “A method for determining surface energy of solids,” *Mater. Sci. Eng.* **11**(6), 311–318 (1973).
81. E. M. Terentjev and S. V. Ahir, “Photomechanical actuation in polymer-nanotube composites,” *Nature Mater.* **4**(6), 491–495 (2005).
82. S. Lu and B. Panchapakesan, “Photomechanical responses of carbon nanotube/polymer actuators,” *Nanotechnology* **18**(30), 305502 (2007).
83. F. M. Sánchez-Arévalo et al., “Photomechanical response of composites based on PDMS and carbon soot nanoparticles under IR laser irradiation,” *Opt. Mater. Express* **5**(8), 1792–1805 (2015).
84. S. Hiremath and S. M. Kulkarni, “Photomechanical actuation of polydimethylsiloxane/carbon black nanocomposite,” *Micro Nano Lett.* **15**(7), 437–440 (2020).

85. S. Ansari, C. Rahima, and M. N. Muralidharan, "Photomechanical characteristics of thermally reduced graphene oxide - polydimethylsiloxane nanocomposites," *Polym. Plast. Technol. Eng.* **52**(15), 1604–1610 (2013).
86. G. Rajitha and R. K. Dash, "Optically transparent and high dielectric constant reduced graphene oxide (RGO)-PDMS based flexible composite for wearable and flexible sensors," *Sens. Actuator A: Phys.* **277**, 26–34 (2018).
87. H. Liu et al., "Illumination-oriented and thickness-dependent photomechanical bilayer actuators realized by graphene-nanoplatelets," *Sens. Actuators A-Phys.* **239**, 45–53 (2016).
88. J. Loomis et al., "Graphene-nanoplatelet-based photomechanical actuators," *Nanotechnology* **23**(4), 045501 (2012).
89. J. E. Mark, *Polymer Data Handbook*, Oxford University Press, New York (1999).
90. "Overview of materials for Fluorinated Ethylene Propylene (FEP), molded/extruded," <https://www.matweb.com/search/DataSheet.aspx?MatGUID=c782af4519d949349d7c771ff6953314&ckck=1> (accessed 12 December 2023).
91. G. Cocchi, M. G. De Angelis, and F. Doghieri, "Solubility and diffusivity of liquids for food and pharmaceutical applications in crosslinked polydimethylsiloxane (PDMS) films: I. Experimental data on pure organic components and vegetable oil," *J. Membr. Sci.* **492**, 600–611 (2015).

Matthew Knitter is an engineering physics undergraduate at Florida Polytechnic University.

Louis Ferreira is an engineering physics undergraduate at Florida Polytechnic University.

D. Ryan Sheffield is an engineering physics undergraduate at Florida Polytechnic University.

Joseph Pusateri is an engineering physics undergraduate at Florida Polytechnic University.

Nathan J. Dawson is an associate professor of engineering physics at Florida Polytechnic University who received his PhD in physics from Washington State University in December, 2010.